processes

MDPI

Article

Study on the Inner Mechanisms of Gas Transport in Matrix for Shale Gas Recovery with In Situ Heating Technology

Zhongkang Li [1], Zantong Hu [1], Ying Li [1], Xiaojun Wu [2,3,*], Junqiang Tian [2,3] and Wenjing Zhou [2,3]

[1] Exploration and Development Integration Center of PetroChina Zhejiang Oilfield Company, Hangzhou 310023, China
[2] School of Petroleum and Natural Gas Engineering, Changzhou University, Changzhou 213164, China
[3] CNPC-CZU Innovation Alliance, Changzhou 213164, China
* Correspondence: xiaojun_wu@cczu.edu.cn

Abstract: In order to improve the productivity of shale gas, in situ heating technology has been applied generally. However, this technology is limited by unknown properties in heated matrix, e.g., permeability. Therefore, a method for measuring the permeability of heated shale matrix particles was designed, and transport tests were conducted on the shale matrix at heating temperatures of 100~600 degrees centigrade. Through fitting the experimental data with numerical simulation results, pore structures and permeabilities at different heating temperature conditions were obtained and the corresponding transport properties were determined. The porosity and pore radius were positively correlated with the heating temperature, while the tortuosity was negatively correlated with the temperature of the heat treatment. Despite the weakening effect of Knudsen diffusion transport, slippage transport played a critical role in the transport function of the heated shale matrix, and the domination became stronger at higher heating temperatures. The study of gas transport in heated shale matrix provides a guarantee for the effective combination of in situ heating technology.

Keywords: shale matrix; gas transport; in situ heating technology; slippage transport; Knudsen diffusion transport

check for updates

Citation: Li, Z.; Hu, Z.; Li, Y.; Wu, X.; Tian, J.; Zhou, W. Study on the Inner Mechanisms of Gas Transport in Matrix for Shale Gas Recovery with In Situ Heating Technology. *Processes* **2024**, *12*, 1247. https://doi.org/10.3390/pr12061247

Academic Editor: Vladimir S. Arutyunov

Received: 20 May 2024
Revised: 11 June 2024
Accepted: 14 June 2024
Published: 18 June 2024

Copyright: © 2024 by the authors. Licensee MDPI, Basel, Switzerland. This article is an open access article distributed under the terms and conditions of the Creative Commons Attribution (CC BY) license (https://creativecommons.org/licenses/by/4.0/).

1. Introduction

Shale gas is an important oil and gas resource for energy worldwide, providing powerful support for social and economic development. Considering its high compactness, in order to improve the productivity of shale gas, in situ heating technology has gradually been applied to increase shale gas production in addition to hydraulic fracturing technology. The study of gas transport in heated shale matrix could help to clarify the permeability increment of heated shale matrix and its impact on gas productivity improvement, providing valuable data for the effective combination of in situ heating technology and supporting technologies [1,2].

Shale gas reservoirs can be difficult to develop, owing to their low permeability and the low abundance of gas [3,4]. In situ heating technology is not only widely used in shale oil development [5–7], but has also been applied constantly in shale gas development [8–10]. Generally, the in situ heating technologies and yield-increasing mechanisms for shale gas and shale oil are consistent and universal [11]. Through heating technology, the organic matter in the shale is decomposed and the inorganic matter is ruptured via heating, and fractures are increased [12].

Compared with matrix acidizing and surfactants, hydraulic fracturing with proppants and in situ heating is more suitable to enhance shale gas recovery, due to the strong fracture-making ability of the process [13]. The created fractures can improve the permeability of shale and reduce the gas transport difficulty from shale matrix to wellbore [14]. Different from hydraulic fracturing, the thermal fractures induced by in situ heating are less likely to reclose due to irreversible pyrolysis of organic matter [15]. For shale gas reservoirs,

microwave heating [10,16,17] and electrical heating technologies [9,18] have been able to effectively increase gas production by more than 5%. The thermal evolution of permeability is the key to the increase in gas production through heated shale, which is worthy of further study [17].

In order to determine the permeability variation characteristics of heated shale, a series of gas transport studies were carried out through measuring the permeability of the shale core plug at different heating temperatures. The permeability was mainly controlled by the pyrolysis of organic matter and the thermal stress fracture of inorganic matter [19,20]. When the temperature exceeded the threshold temperature, the permeability increased rapidly to a value nearly 100 times the original [21]. The variation of shale permeability is slight when the heating temperature is lower than 200 degrees centigrade, and there is a process decreasing and then increasing the heating temperature to higher than 200 degrees centigrade [22–24]. The pyrolysis and thermal cracking mentioned in studies appear in the shale matrix. However, the shale core plug used in the measurement of permeability contained matrix and fractures. It is impossible to establish the relationship between the variations in heated shale matrix and matrix permeability based on shale core plug samples. In addition, due to the nanoscale pore size of shale matrix [25,26], the matrix permeability is controlled through both slippage effect and Knudsen diffusion [27]. Gas flow tests in shale core plug are more likely to reflect the macro flow in fractures, rather than the micro flow in the shale matrix, consisting of slippage flow and Knudsen diffusion flow.

For the effective determination of shale matrix permeability, the shale samples, which were regarded as shale matrix without fractures, were crushed to particles in advance [28–30]. This method has been standardized and is referred to as the Gas Research Institute (GRI) method [31,32]. In hermetic equipment, gas expanded into the evacuated shale matrix particles, and the corresponding pressure drop during this process was recorded as experimental data. These data could be fitted with mathematical models, and the key transport parameters could be obtained for further matrix permeability studies. For a more accurate fitting, the slippage effect and Knudsen diffusion were applied to the mathematical model [33]; the microscale slippage flow and Knudsen diffusion flow in heated shale matrix have seldom previously been studied. The detailed method is introduced in Section 2. To improve gas supplement speed and ensure the accuracy of experimental data processing, an automatic gas supplement and pressurization (AGSP) system [34] and an apparent permeability model [33] were applied to improve the GRI method. Based on the improved GRI method, the permeability of heated shale matrix was obtained, supplying transport parameters for the application of in situ heating technology on heated shale gas reservoirs. Meanwhile, it was necessary to avoid the pollution of organic matter cracking products on the experimental equipment.

In this context, there have been insufficient experimental studies on shale matrix particles, and the influence of heating temperature on matrix permeability is still unclear, which stands adverse to the application of in situ heating technology. In this study, the equipment for the GRI method was further improved, and transport tests were conducted on the shale matrix at 100~600 degrees centigrade heating temperature conditions. Through fitting the experimental data, pore structures and permeabilities at different heating temperature conditions were obtained and the corresponding slippage flow and Knudsen diffusion flow properties were determined, revealing the dynamic transport mechanisms. This study provides a theoretical basis for the intelligent and systematic development of heated shale gas reservoirs.

2. Materials and Methods

2.1. Experimental Samples

As a typical rock sample of shale gas reservoir, a sample of Wufeng–Longmaxi Formation shale was selected to study the transport ability of heated shale matrix [15]. In order to compare the transport characteristics of shale at different heating temperatures, 11 shale samples were heated in the range of 100~600 degrees centigrade at 50 degree intervals in

high temperature heating furnace. Aiming to avoid the effect of fracture on the permeability of shale matrix, the shale was crushed to 20~30 mesh before heat treatment [35]. All the crushed samples were obtained from a single shale rock and were mixed evenly in advance to reduce the difference of properties in each sample. The shale sample was to investigate the related transport without heating treatment at 30 degrees centigrade using the GRI method; the porosity obtained was 0.038, the pore radius was 1.5 nm, and the tortuosity was 37 [34]. The mass proportion of TOC in shale samples was 3.61%, based on carbon and sulfur analysis. Quartz accounted for the largest proportion, 37.9%, and calcite accounted for 16.3% [36], according to the X-ray diffraction test.

2.2. Experimental Equipment and Method

Aiming to conduct accurate permeability testing of the heated shale matrix, a corresponding experimental device was designed. The device was characterized by two vents controlled via Valve 3 and Valve 5 and a vacuum port controlled via Valve 4 (Figure 1). The sample cell containing the sample was pre-placed in a thermostatic oven. In the high-temperature heating stage (higher than 400 degrees centigrade), the moisture and hydrocarbon gases produced by the pyrolytic shale matrix would easily pollute the outgassing line controlled via Valve 3 only. To prevent this pollution, the two outgassing lines controlled via Valve 3 and Valve 5 were used in the heating round and transmission test round, respectively. The polluted outgassing line controlled via Valve 3 was not utilized in the transmission test round, while the contaminated line controlled via Valve 5 was utilized to prevent the water and hydrocarbon gases in the line (controlled via Valve 3) from refluxing to the shale matrix sample and interfering with the sample transmission test results.

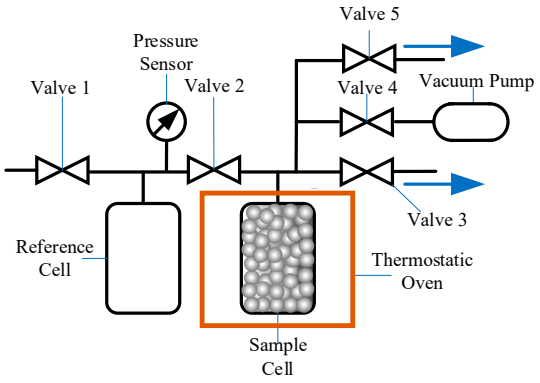


Figure 1. Equipment for transport testing of heated shale matrix.

To obtain the experimental data on gas transport in the heated shale matrix particles, the specific operating steps were as follows:

(1) Valves 1, 2, 4, and 5 were closed in advance and Valve 3 was opened.The thermostatic oven was turned on to heat the shale matrix in the sample cell. The temperature was raised to the target temperature at a rate of 10 degrees centigrade/min and maintained for 4 h.

(2) Then, the sample was cooled naturally to a constant temperature of 30 degrees centigrade. In the natural cooling process, when the temperature reached 80 degrees centigrade, Valve 3 was turned off quickly, Valves 2 and 4 were turned on, and the vacuum was started and run for 12 h. In the vacuum, in time, the contact time between shale sample and external air was reduced, and a secondary reaction between pyrolysis matrix and oxygen and water adsorption was avoided.

(3) After vacuuming, Valves 2 and 4 were turned off. Valve 1 was opened, and after using helium cylinders to supply the reference cell to the target pressure [34], Valve 1 was closed.

(4) Valve 2 was opened to let the gas in the reference cell release to the sample cell. The pressure in the system varied sharply due to the gas release and dropped gradually due to the entering of the gas into the shale matrix. The dynamic pressure drop data needed for the experiment were recorded with the pressure sensor to obtain the required experiment data.

The parameters of sample refilling degree, particle density and total particle volume were the same as the pilot study [34], i.e., 39.331%, 2.636 g/mL, and 17.052 mL. From the beginning of the vacuum to the end of the experiment, the thermostatic oven maintained the temperature of the sample cell at 30 degrees centigrade. Based on the numerical model used in the pilot study [33], according to the experimental temperature and pressure data, the microscopic apparent permeability considering the slippage effect and Knudsen diffusion characteristics was obtained through fitting porosity ϕ, transmission pore radius r, and tortuosity τ.

In order to deal with the experimental data effectively, the following numerical simulation expressions were used [33]:

$$p_i^{n+1} = \frac{Z_i^n \Delta t}{\phi (i\Delta r)^2} \left[\begin{array}{l} \left(i+\frac{1}{2}\right)^2 \frac{k_{a_{i+\frac{1}{2}}}^n}{\mu_{i+\frac{1}{2}}^n C_{g_{i+\frac{1}{2}}}^n} \left(\left(\frac{p}{Z}\right)_{i+1}^n - \left(\frac{p}{Z}\right)_i^n \right) - \\ \left(i-\frac{1}{2}\right)^2 \frac{k_{a_{i-\frac{1}{2}}}^n}{\mu_{i-\frac{1}{2}}^n C_{g_{i-\frac{1}{2}}}^n} \left(\left(\frac{p}{Z}\right)_i^n - \left(\frac{p}{Z}\right)_{i-1}^n \right) \end{array} \right] + p_i^n \quad (1)$$

where p is the pressure of helium, ka is the apparent permeability, n is the nth time step, and Z, μ, and C_g are gas property coefficients, which are compressibility factor, viscosity, and compression coefficients. ka can be expressed as [37,38]:

$$k_a = k_s \omega_s + k_k \omega_k \quad (2)$$

where k_s and k_k are permeabilities for slippage flow and Knudsen diffusion, and ω_s and ω_k are weight factors of slippage flow and Knudsen diffusion.

For Equation (1), divide the single preheated and cooled shale matrix particle into m intervals in the radial direction, and designate a certain interval as i, as shown in Figure 2.

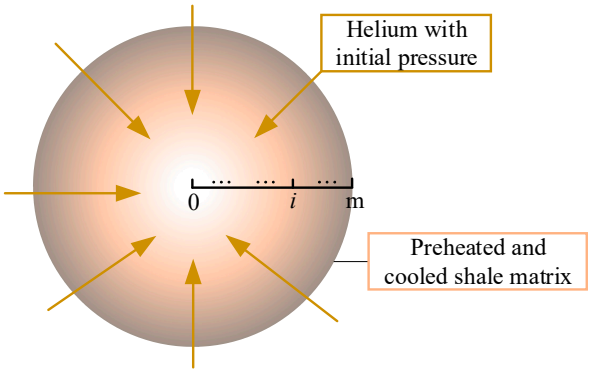


Figure 2. Differential processing of heated shale matrix particle.

3. Results and Discussion

3.1. Experimental Results and Analyses

In order to study the characteristics of gas transport in heated shale matrix, the pressure drop curves of initial pressures 3 MPa, 4 MPa, 5 MPa, and 6 MPa in the heating temperature range of 100~600 degrees centigrade were obtained based on the shale matrix testing device, as shown in Figure 3. The pressure drop curves of 3 MPa, 4 MPa, and 5 MPa were selected to fit the shale matrix parameters, ϕ, r, and τ, and the fitting verification was carried out under 6 MPa initial pressure. It was found that, for heating temperatures of 100~600 degrees centigrade, the accuracy of the fitting results' ϕ, r, and τ parameters was high. In Figure 3, the fitting results for 100, 200, 300, 400, 500, and 600 degrees centigrade

are shown. Based on the coefficient of determination values, R^2, the simulated pressure drop curves corresponded well to the experimental pressure drop data under 3 MPa, 4 MPa, and 5 MPa pressures (Figure 3a–c). Under the condition of 6 MPa pressure, the simulated pressure drop curve based on the same fitting parameters was still in good agreement with the experimental pressure drop curve (Figure 3d). The values of R^2 under 3 MPa, 4 MPa, 5 MPa, and 6MPa pressures were all larger than 0.8. The permeability of the shale matrix at different heat treatment temperatures was further calculated with Equation (2). The specific simulation results are shown in Figure 4.

For higher heating temperatures, the time for the pressure drop to stabilize was shorter, and the pressure drop amplitude was larger, indicating that the gas transport velocity and porosity in the matrix increased with the increase in treatment temperature. It should be noted that due to the limitations of the experimental equipment and operating errors, the initial pressure of the experiment could not be strictly controlled to 3 MPa, 4 MPa, 5 MPa, and, 6 MPa, and could only be set close to the target pressures of the experiment. This operation did not affect the accuracy, and the theoretical simulation pressures utilized were consistent with the actual experimental pressure.

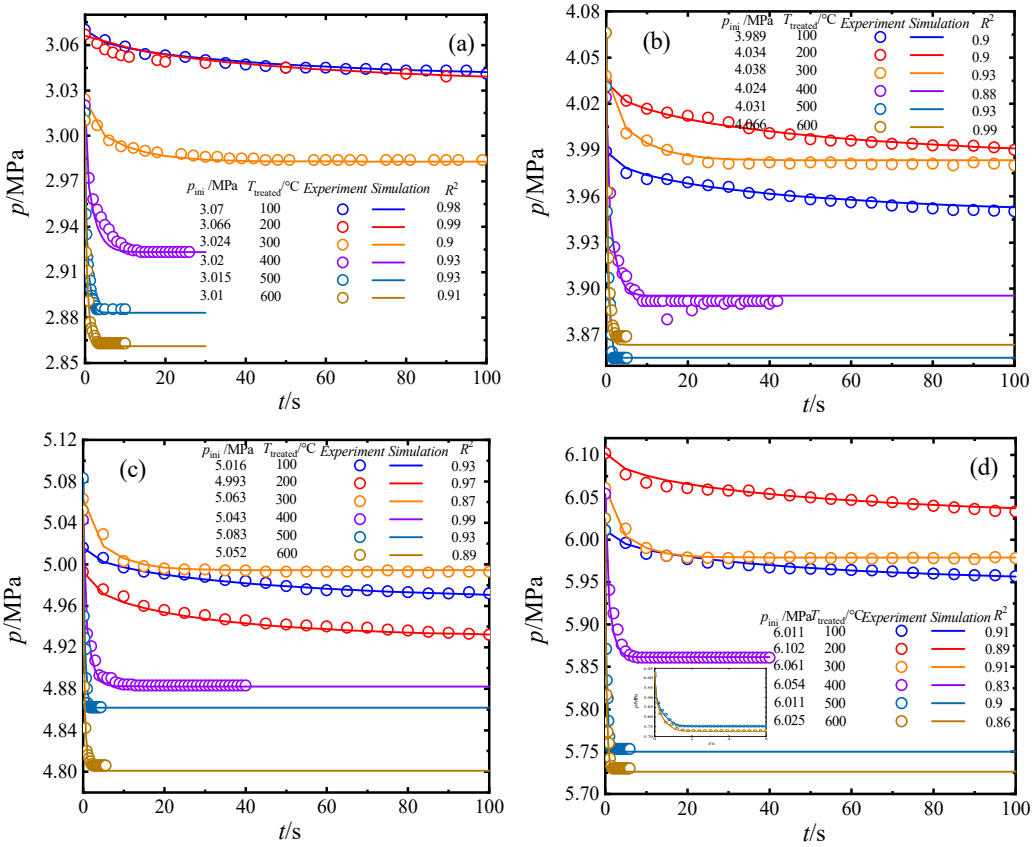


Figure 3. Experimental fitting and verification of transport in heated shale matrix: (**a**–**c**) represent the curve fittings for 3, 4, and 5 MPa conditions; (**d**) represents the verification at 6 MPa.

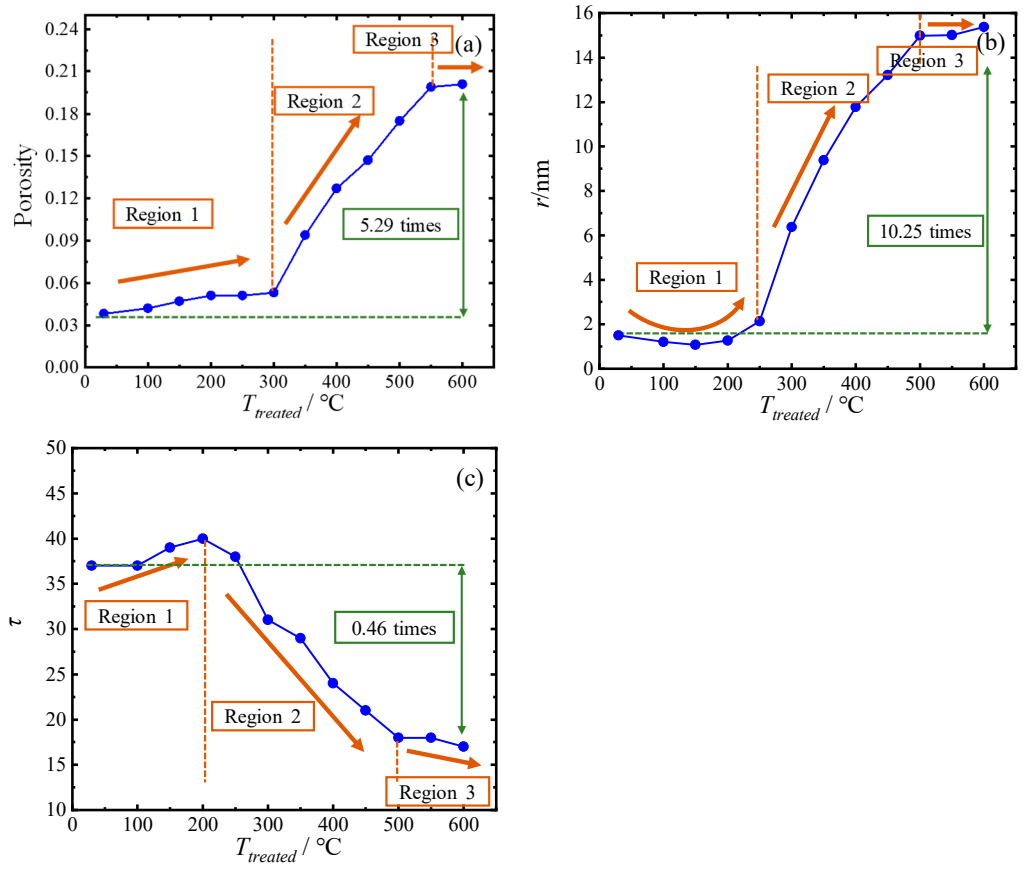


Figure 4. Relationships of porosity (**a**), pore radius (**b**), and tortuosity (**c**) with heating temperature.

The fitting results show that the porosity and pore radius were approximately positively correlated with the heat treatment temperature (Figure 4a,b), while the tortuosity was negatively correlated with the heat treatment temperature (Figure 4c). According to the characteristics of the relationship curve, porosity, pore radius, and tortuosity could be divided into three stages with the increase in heating temperature, as shown in Figure 4, corresponding to the three-stage change in the pore structure of oil shale [39–41]. In the three stages of <300, 300~550, and >550 degrees centigrade, the pore structure was mainly controlled through inorganic thermal stress, pyrolysis, and inorganic cracking. Moreover, as a reference for the analysis of shale pore structure, the pyrolysis of shale organic matter can be divided into three stages [20]: an unpyrolytic stage (<300 degrees centigrade), a pyrolytic stage (300 degrees centigrade) and the end of the pyrolytic stage (>450 degrees centigrade). Due to the differences between shale samples, the temperatures of each stage are different, but the basic mechanism is the same [6].

Specifically, based on this study, the thermal evolution characteristics of the pore structures of Wufeng–Longmaxi shale samples were determined. When the heating temperature was lower than 300 degrees centigrade, the porosity increased slowly. In this temperature range, there was no pyrolysis, and the porosity was dominated by quartz thermal stress brittleness (quartz mass accounted for 37.9%). Due to the continuous formation of organic matter pyrolysis products, the pore space expanded rapidly, and the porosity increased rapidly from 300 to 550 degrees centigrade. Similarly, due to the generation of new pores and the enhancement of connectivity, the pore size increased rapidly and the tortuosity decreased rapidly. When the temperature was higher than 550 degrees centigrade, the shale was fully pyrolyzed and the porosity tended to be stable.

In the range below 250 degrees centigrade, the pore radius decreased at first and then increased with the increase in heating temperature. This was because the width of the micro-cracks produced by the thermal stress at low temperature was narrower than

the original pore diameter, which reduced the overall pore size. With the increase in temperature, the width of microcracks produced by thermal stress gradually became larger than the original pore diameter. Owing to the domination of quartz in the shale sample and the strong thermal stress, the pore size increased rapidly after 250 degrees centigrade. The growing complexity of pore structures was also observed in previous research [23], while the corresponding variation of tortuosity remained unknown. In the current study, the tortuosity increased briefly when the temperature was lower than 200 degrees centigrade. The microcracks caused by low temperature thermal stress increased the connectivity of the original pores, while the small width of the cracks increased the complexity of the interpore connectivity. Compared with the initial values, the porosity and pore radius increased by 5.29 times and 10.25 times, respectively, and the tortuosity decreased to 0.46 times its original value at 600 degrees centigrade. Porosity is mainly affected by the single factor of organic matter pyrolysis. However, due to the comprehensive effect of the thermal stress of inorganic minerals and the pyrolysis of organic matter, the variation range of the pore radius was much larger than that of porosity or tortuosity.

3.2. Influence of Heating Temperature on Shale Matrix Transport

To analyze the transport characteristics of shale matrix particles in micropores at different heating temperatures, initial pressures of 1 MPa, 5 MPa, and 9 MPa were selected for investigation. In the heating temperature range of 100~600 degrees centigrade, the fluid transport in the matrix micropores was dominated by transition flow (Figure 5). Within the transition flow, slippage flow and Knudsen diffusion flow were both present ($0.1 \leq kn \leq 10$) [42]. At the same heating temperature, the greater the pressure, the smaller is the Knudsen number [43,44]. Knudsen diffusion single flow was present in the matrix pores at lower temperatures (<200 degrees centigrade) and lower pressure (<1 MPa), and slippage single flow was present in the matrix pores at higher temperatures (>400 degrees centigrade) and higher pressure (>9 MPa). At 150 degrees centigrade, the Knudsen number reached its maximum value, corresponding to the minimum point of the pore radius (Figure 4b), reflecting the strong correlation between the Knudsen number and the pore radius. Above 150 degrees centigrade, the Knudsen number under each pressure condition decreased rapidly, approaching 0.1, and the transition flow gradually approached the slip flow.

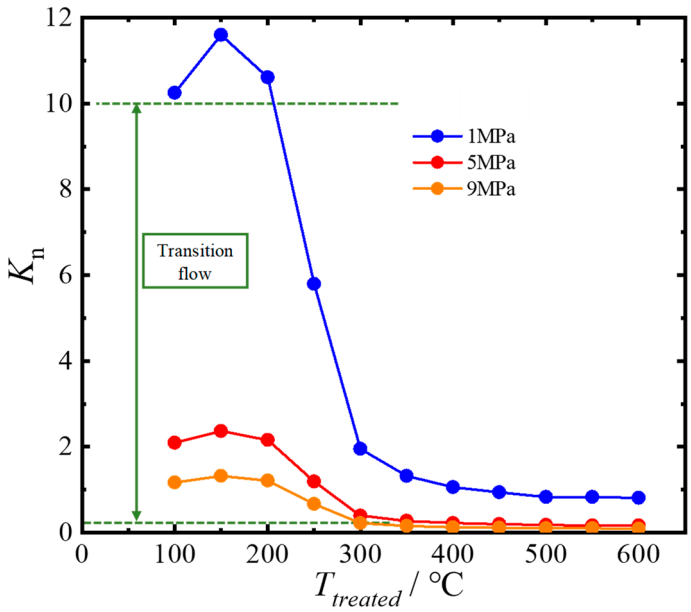


Figure 5. Relationship of Knudsen number with heating temperature.

For different pressure conditions, the variations of slippage permeability and Knudsen diffusion permeability are similar, and both increase with the rising of heating temperature

(Figure 6). According to the definition of slippage permeability and Knudsen diffusion permeability [45], both permeabilities are positively correlated with porosity and pore radius, and negatively correlated with tortuosity. Therefore, there are positive correlations of porosity, pore radius with heating temperature (Figure 4a,b) and negative correlation of tortuosity with heating temperature (Figure 4c), stimulating the positive correlations of slippage permeability and Knudsen diffusion permeability with heating temperature. Under the condition of lower than 300 degrees centigrade, the slippage permeability and Knudsen diffusion permeability increase slowly, due to the slight increases of porosity, pore radius and tortuosity. When the temperature is higher than 300 degrees centigrade, the increases of porosity, pore radius, and tortuosity are expanded, resulting in the rapid growth of slippage permeability and Knudsen diffusion permeability. There is a break point at 500 degrees centigrade, and the permeability continues to increase, which is consistent with the variation of tortuosity at 500 degrees centigrade. Therefore, at the heat treatment temperature above 500 degrees centigrade, the changes in slippage permeability and Knudsen diffusion permeability are mainly controlled by tortuosity.

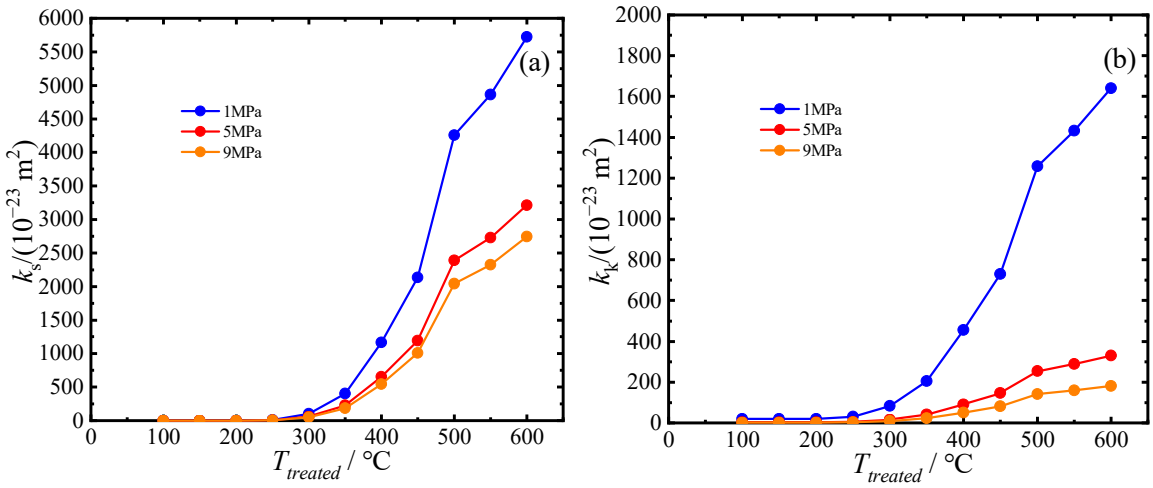


Figure 6. Relationships of slippage permeability (**a**), and Knudsen diffusion permeability (**b**), with heating temperature.

The weight factors of slippage and Knudsen diffusion were calculated according to the single factor of the Knudsen number, which represents the probability of transmission of fluid molecules in the forms of slippage and Knudsen diffusion [46], respectively. Weight factors can be used to characterize the intensities of slippage transport and Knudsen diffusion transport. Under the same conditions, the sum of weight factors of slippage and Knudsen diffusion is 1. As shown in Figure 7a, affected by the relationship of the Knudsen number and the heating temperature, the slippage weight factor increased in an "S" shape with the heating temperature. Accordingly, the Knudsen diffusion weight factor decreased with an inverse "S" shape. At the same heating temperature, with higher pressure, the weight factor of slippage transmission increased, and the probability of slippage transmission became stronger. The variation in proportions for slip flow and Knudsen diffusion flow in the total transmission was similar to the weight factors (Figure 7b), indicating the dominant role of the weight factor on the total transmission mechanism. In the low temperature range (<200 degrees centigrade), the slippage transport ratio was basically less than 0.5, dominated by Knudsen diffusion, while in the high temperature range (>400 degrees centigrade), the slippage transport ratio was basically larger than 0.5, dominated by slippage flow.

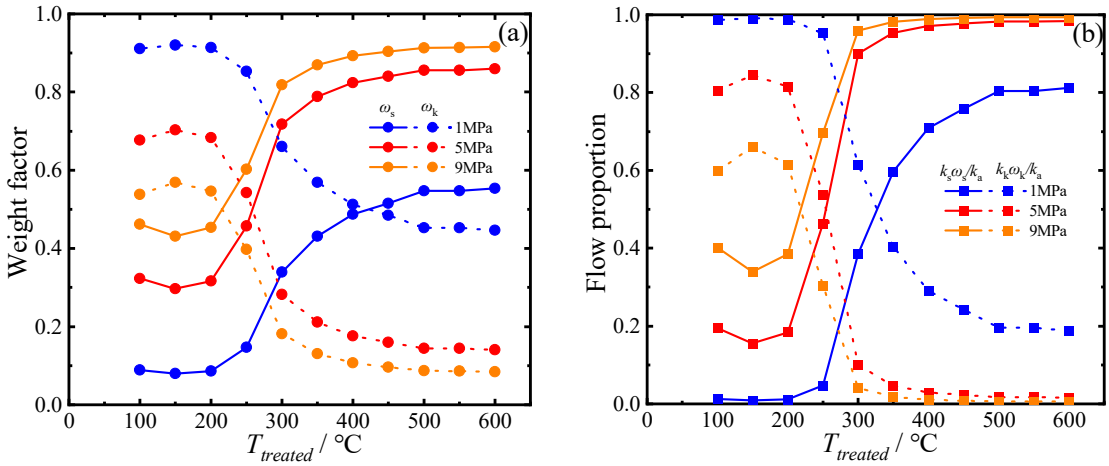


Figure 7. Relationships of weight factors (**a**) and flow proportions (**b**) with heating temperature. The parameters, ω_s and $k_s\omega_s/k_a$, were represented by solid lines with solid circle and square, separately. The parameters, ω_k and $k_k\omega_k/k_a$, were represented by dashed lines with solid circle and square, separately.

Based on the relationships of slippage permeability, Knudsen diffusion permeability, and corresponding weight factors with heating temperature, according to Equation (2), the relationship of total apparent permeability with heating temperature was obtained (Figure 8). Based on the core plug sample, only large scale fractures increased the permeability, and the impact of pore structure variations in the matrix was ignored [19]. In this research, the temperature had an obvious impact on the total matrix particle permeability due to variations in the pore structure. The shape of the total permeability curve was similar to that for the slippage permeability, further implying that the slippage transport played a critical role in the transport in the heated shale matrix. In the low temperature range (below 300 degrees centigrade), there was a minimum point of total permeability, reflecting the influence of the minimum value of the pore radius on the total permeability (Figure 4b). It was found in previous research on a Wufeng–Longmaxi shale core plug sample [15] that the permeability increased rapidly above 400 degrees centigrade, higher than the shale matrix in the current study, as shown in Figure 8. Therefore, the matrix permeability may be more sensitive to the temperature of the core.

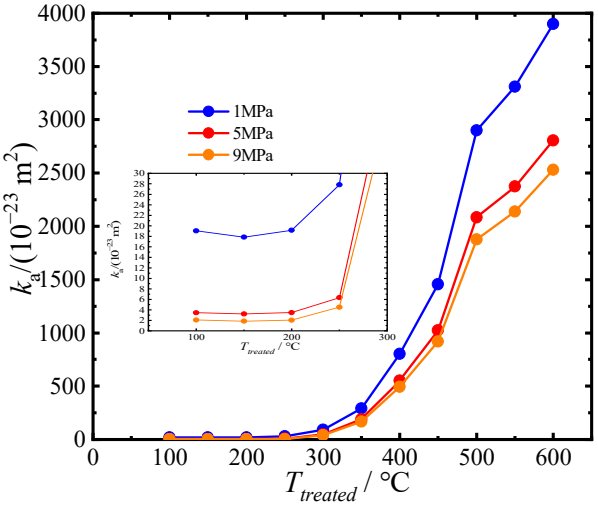


Figure 8. Relationship of apparent permeability with heating temperature.

Owing to the break points of slippage permeability and Knudsen diffusion permeability at 500 degrees centigrade, the total permeability also showed a break point at 500 degrees

centigrade, and it continued to increase with the increase in heating temperature. In spite of the domination of slippage flow, Knudsen diffusion flow could not be ignored. The existence of Knudsen diffusion transport weakened the dominant role of slippage transport. The lower the heating temperature, the stronger was the weakening effect. As a result, the total permeability was lower than the slippage permeability in the whole temperature range. These novel findings about apparent permeability will be beneficial to improving the accuracy of in situ heating technology.

3.3. Dynamic Transport in Heated Shale Matrix

For the study of the dynamic transport characteristics in the actual heated shale matrix, the distribution characteristics of pressure, Knudsen number, apparent permeability and slippage permeability in shale matrix particles at heating temperatures of 200 and 400 degrees centigrade and 5 MPa pressure were analyzed, as shown in Figures 9 and 10. At heating temperatures of 200 and 400 degrees centigrade, the matrix was in unpyrolytic and pyrolytic conditions, respectively. The zero point of the abscissa represents the center of the shale matrix, and the gas transports from the right end of the abscissa to the left end, representing the process of gas entering the shale matrix particle.

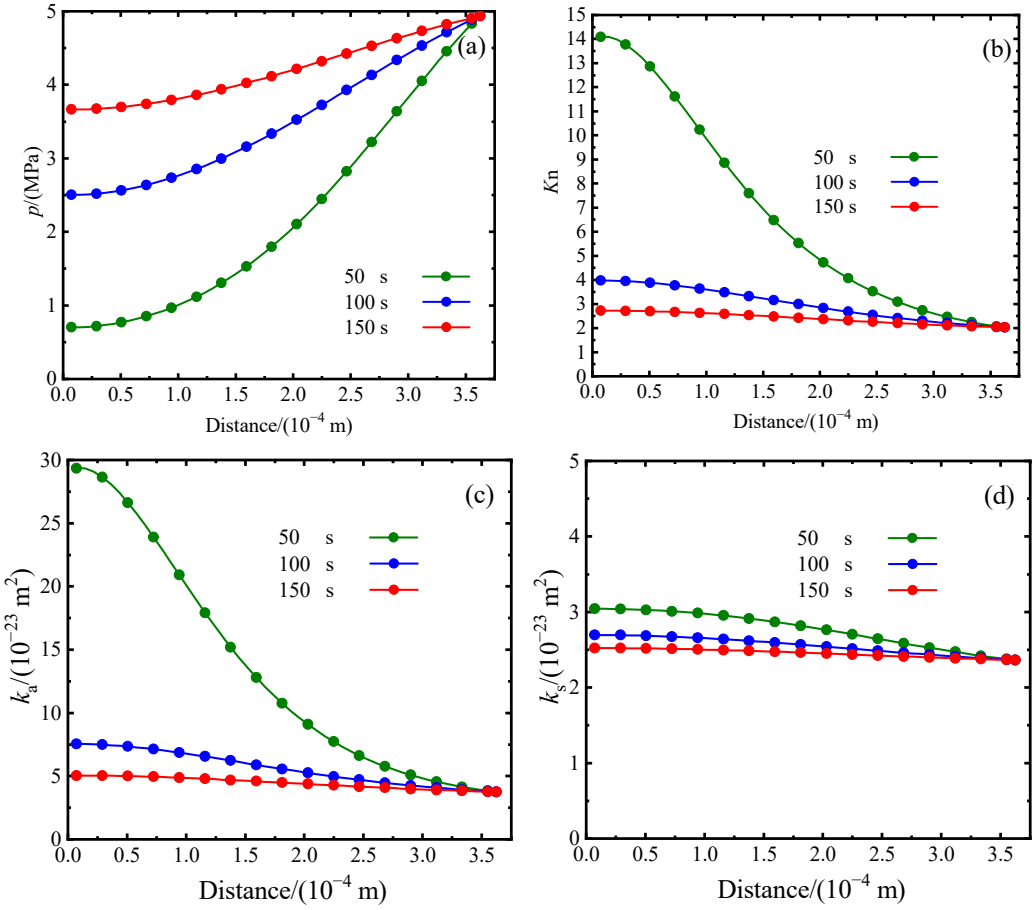


Figure 9. Distributions of pressure (**a**), Knudsen number (**b**), apparent permeability (**c**) and slippage permeability (**d**) of shale matrix particle at 200 degrees centigrade heating temperature.

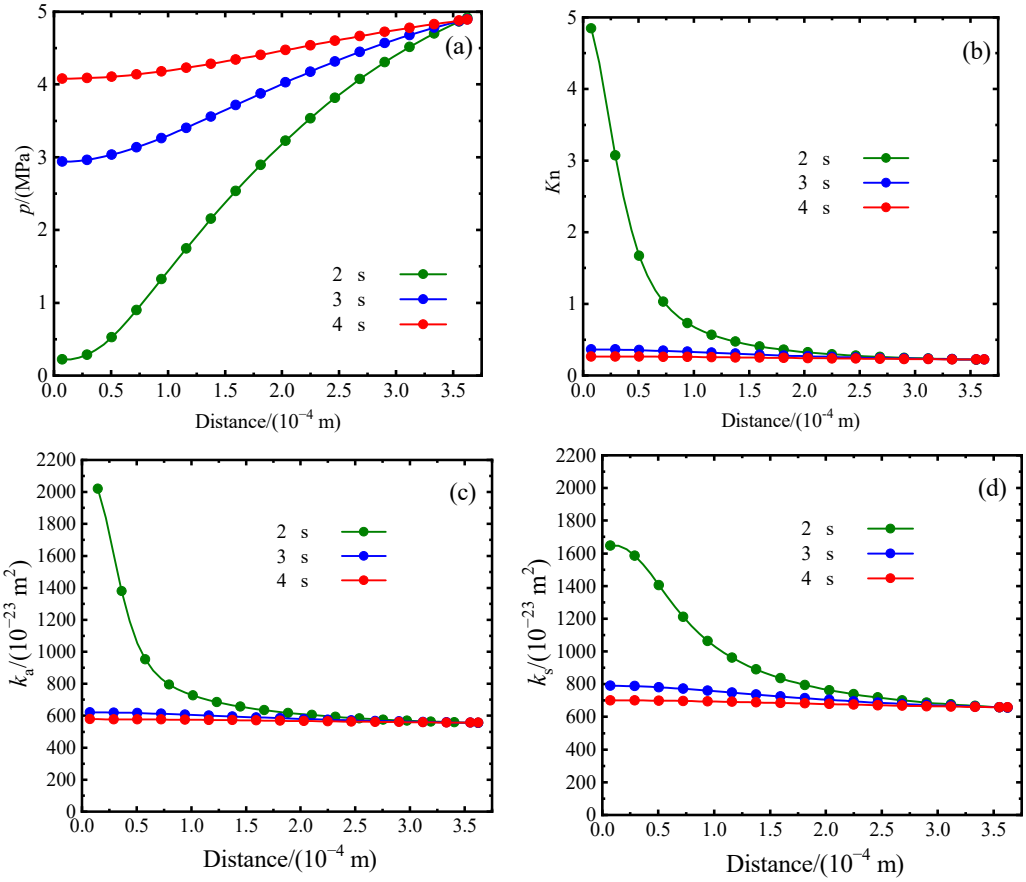


Figure 10. Distributions of pressure (**a**), Knudsen number (**b**), apparent permeability (**c**), and slippage permeability (**d**) of shale matrix particles for 400 degrees centigrade heating temperature.

At the heating temperature of 200 degrees centigrade, the pressure in the shale matrix increased gradually with the gas transporting from the surface of the shale matrix particles to the center (Figure 9a). Closer to the center of the particles, the pressure increased faster. Therefore, in the center of the matrix particles, the pressure distribution appeared relatively gentle. In the process of gas transport, the Knudsen number at each position of the matrix particle was much larger than 0.1, and the Knudsen number near the particle center was larger than 10 at 50 s (Figure 9b). The results showed that there was Knudsen diffusion flow in the matrix at the heating temperature of 200 degrees centigrade, but the transition flow was still in a dominant role. As time passed, the Knudsen diffusion flow at the center of the particles developed into transition flow.

At the same time, closer to the particle center, the higher apparent permeability was beneficial to the gas transfer from the high pressure area to the low pressure area (Figure 9c). Corresponding to the Knudsen number distribution, the apparent permeability at the center of the particles decreased gradually, and the permeability difference between the high pressure zone and the low pressure zone diminished. In addition, the transmission speed of the gas transport leading edge also decreased. The distribution of slippage permeability and shape of the variation with time (Figure 9d) were quite different from the apparent permeability, indicating that, at the heat treatment temperature of 200 degrees centigrade, the dynamic transport in the shale matrix was dominated by Knudsen diffusion rather than slippage.

At the heat treatment temperature of 200 degrees centigrade, the gas in the shale matrix was transported from the high pressure area to the low pressure area. Owing to the higher permeability in the low pressure area, the pressure rising speed appeared higher than that in the high pressure area. With the continuous transport of gas, the pressure in the matrix increased integrally, and the Knudsen diffusion flow completely transformed

into transition flow. Thus, the permeability distribution appeared gradual and smooth and reduced the gas transport speed.

At the 400 degrees centigrade heating temperature, the shale matrix was pyrolyzed, the porosity and pore radius greatly increased, and the tortuosity decreased, resulting in much a higher apparent permeability value than the shale matrix heated at 200 degrees centigrade (Figure 10c). The gas transport process was significantly shortened, and the pressure lifting speed in the matrix particles was accelerated. The pressure distribution in the matrix particles at 400 degrees centigrade for 2 s was similar to that at 200 degrees centigrade for 50 s (Figure 10a). However, in spite of the similar pressure distribution, the Knudsen number decreased and was close to 0.1 in the area of high pressure (Figure 10b). At the heating temperature of 400 degrees centigrade, the gas transport in the shale matrix was closer to the characteristics of slippage. Generally, it is believed that small-scale variations in gas transport in heated shale are not large enough to enhance the recovery [13]. However, positive transformation of the transmission mechanism could bring more gas flowing to the wellbore, which cannot be ignored. At 3 s and 4 s, the distribution of Knudsen number in the whole particle varied slightly, close to 0.1. Correspondingly, the apparent permeability in the low-pressure area was much higher than that in the high-pressure area at 2 s, and the apparent permeability distribution was gentler at 3 s and 4 s (Figure 10c). The distribution pattern of the slippage permeability was similar to that of the apparent permeability, indicating that slippage permeability had a greater contribution to apparent permeability.

4. Conclusions

For the study of gas transport in heated shale matrix, experimental and theoretical investigations were conducted, providing an opportunity to combine in situ heating technology and supporting technologies. The conclusions are given below.

The experimental transport data for heated shale matrix fitted well with the numerical model. The pore structures at each heating temperature (100~600 degrees centigrade) were obtained successfully, and the total permeability was further calculated. The porosity and pore radius were positively correlated with the heating temperature, while the tortuosity was negatively correlated with the heat treatment temperature. Compared with the initial values, the porosity and pore radius increased by 5.29 times and 10.25 times respectively, and the tortuosity decreased to 0.46 times its original value at 600 degrees centigrade. Porosity, pore radius, and tortuosity variations could be divided into three stages due to the thermal stress of inorganic matter and organic matter pyrolysis caused by the heat treatment.

The total permeability was lower than the slippage permeability in the 100~600 degrees centigrade temperature range. Slippage transport plays a critical role in the transport of heated shale matrix. The existence of Knudsen diffusion transport weakened the dominant role of slippage transport, and they both had break points at 500 degrees centigrade. The lower the heating temperature, the stronger was the weakening effect. There was Knudsen diffusion flow in the matrix at the heating temperature of 200 degrees centigrade, but the transition flow was still in a dominant role. As time passed, the Knudsen diffusion flow at the center of the particles developed into transition flow. At a heating temperature of 400 degrees centigrade, slippage permeability had a greater contribution to apparent permeability.

Author Contributions: Conceptualization, Z.L. and X.W.; Methodology, Z.L., Z.H. and Y.L.; Data curation, X.W. and J.T.; Writing—original draft, Z.H. and X.W.; Writing—reviewing and editing, Z.H. and W.Z.; Investigation, Z.L. and Y.L. All authors have read and agreed to the published version of the manuscript.

Funding: This research received no external funding.

Data Availability Statement: Data are contained within the article.

Conflicts of Interest: Authors Zhongkang Li, Zantong Hu and Ying Li were employed by the company, PetroChina Zhejiang Oilfield Company. The remaining authors declare that the research was conducted in the absence of any commercial or financial relationships that could be construed as a potential conflict of interest.

References

1. Liu, J.; Bai, X.; Elsworth, D. Evolution of pore systems in low-maturity oil shales during thermal upgrading—Quantified by dynamic SEM and machine learning. *Pet. Sci.* **2023**, in press. [CrossRef]
2. Liu, Y.; Yao, C.; Liu, B.; Xuan, Y.; Du, X. Performance Prediction and Heating Parameter Optimization of Organic-Rich Shale In Situ Conversion Based on Numerical Simulation and Artificial Intelligence Algorithms. *ACS Omega* **2024**, *9*, 15511–15526. [CrossRef] [PubMed]
3. Yang, F.; Xu, S.; Hao, F.; Hu, B.; Zhang, B.; Shu, Z.; Long, S.J.M.; Geology, P. Petrophysical characteristics of shales with different lithofacies in Jiaoshiba area, Sichuan Basin, China: Implications for shale gas accumulation mechanism. *Mar. Pet. Geol.* **2019**, *109*, 394–407. [CrossRef]
4. Zhijun, J.; Rukai, Z.; Liang, X.; Yunqi, S. Several issues worthy of attention in current lacustrine shale oil exploration and development. *Pet. Explor. Dev.* **2021**, *48*, 1471–1484.
5. Bauman, J.H.; Deo, M. Simulation of a conceptualized combined pyrolysis, in situ combustion, and CO_2 storage strategy for fuel production from Green River oil shale. *Energy Fuels* **2012**, *26*, 1731–1739. [CrossRef]
6. Qi, C.; Liu, J.; Liu, K.; Tuo, J.; Sun, L.; Huang, W.; Li, S.; Regenauer-Lieb, K. Thermal pyrolysis-induced shale micro-cracks: 3D characterization and implication for reservoir stimulation. *Gas Sci. Eng.* **2023**, *118*, 205107. [CrossRef]
7. Hu, H.; Zhang, T.; Wiggins-Camacho, J.D.; Ellis, G.S.; Lewan, M.D.; Zhang, X. Experimental investigation of changes in methane adsorption of bitumen-free Woodford Shale with thermal maturation induced by hydrous pyrolysis. *Mar. Pet. Geol.* **2015**, *59*, 114–128. [CrossRef]
8. Liu, J.; Liang, X.; Xue, Y.; Yao, K.; Fu, Y. Numerical evaluation on multiphase flow and heat transfer during thermal stimulation enhanced shale gas recovery. *Appl. Therm. Eng.* **2020**, *178*, 115554. [CrossRef]
9. Wang, Y.; Liao, B.; Qiu, L.; Wang, D.; Xue, Q. Numerical simulation of enhancing shale gas recovery using electrical resistance heating method. *Int. J. Heat Mass Transf.* **2019**, *128*, 1218–1228. [CrossRef]
10. Chen, T.; Zheng, X.; Qiu, X.; Feng, X.-T.; Elsworth, D.; Cui, G.; Jia, Z.; Pan, Z. Experimental study on the feasibility of microwave heating fracturing for enhanced shale gas recovery. *J. Nat. Gas Sci. Eng.* **2021**, *94*, 104073. [CrossRef]
11. Hu, L.; Li, H.; Babadagli, T.; Xie, X.; Deng, H. Thermal stimulation of shale formations by electromagnetic heating: A clean technique for enhancing oil and gas recovery. *J. Clean. Prod.* **2020**, *277*, 123197. [CrossRef]
12. Pan, Y.; Zheng, L.; Liu, Y.; Wang, Y.; Yang, S. A review of the current status of research on convection-heated in situ extraction of unconventional oil and gas resources (oil shale). *J. Anal. Appl. Pyrolysis* **2023**, *175*, 106200. [CrossRef]
13. Kang, Y.; Chen, M.; You, L.; Li, X. Laboratory measurement and interpretation of the changes of physical properties after heat treatment in tight porous media. *J. Chem.* **2015**, *2015*, 341616. [CrossRef]
14. Zhao, X.; Rui, Z.; Liao, X.; Zhang, R. The qualitative and quantitative fracture evaluation methodology in shale gas reservoir. *J. Nat. Gas Sci. Eng.* **2015**, *27*, 486–495. [CrossRef]
15. Kang, Y.; Chen, M.; Chen, Z.; You, L.; Hao, Z. Investigation of formation heat treatment to enhance the multiscale gas transport ability of shale. *J. Nat. Gas Sci. Eng.* **2016**, *35*, 265–275. [CrossRef]
16. Liu, J.; Wang, J.; Leung, C.; Gao, F. A fully coupled numerical model for microwave heating enhanced shale gas recovery. *Energies* **2018**, *11*, 1608. [CrossRef]
17. Fianu, J.; Gholinezhad, J.; Hassan, M. Thermal simulation of shale gas recovery involving the use of microwave heating. *J. Pet. Sci. Eng.* **2020**, *186*, 106768. [CrossRef]
18. Wang, Y.-D.; Wang, X.-Y.; Xing, Y.-F.; Xue, J.-K.; Wang, D.-S. Three-dimensional numerical simulation of enhancing shale gas desorption by electrical heating with horizontal wells. *J. Nat. Gas Sci. Eng.* **2017**, *38*, 94–106. [CrossRef]
19. Wei, Z.; Sheng, J. Study of thermally-induced enhancement in nanopores, microcracks, porosity and permeability of rocks from different ultra-low permeability reservoirs. *J. Pet. Sci. Eng.* **2022**, *209*, 109896. [CrossRef]
20. Xu, S.; Sun, Y.; Yang, Q.; Wang, H.; Kang, S.; Guo, W.; Shan, X.; He, W. Product migration and regional reaction characteristics in the autothermic pyrolysis in-situ conversion process of low-permeability Huadian oil shale core. *Energy* **2023**, *283*, 128525. [CrossRef]
21. Li, X.; You, L.; Kang, Y.; Liu, J.; Chen, M.; Zeng, T.; Hao, Z. Investigation on the thermal cracking of shale under different cooling modes. *J. Nat. Gas Sci. Eng.* **2022**, *97*, 104359. [CrossRef]
22. Zhao, J.; Kang, Z. Permeability of oil shale under in situ conditions: Fushun oil shale (China) experimental case study. *Nat. Resour. Res.* **2021**, *30*, 753–763. [CrossRef]
23. Liu, J.; Xue, Y.; Zhang, Q.; Yao, K.; Liang, X.; Wang, S. Micro-cracking behavior of shale matrix during thermal recovery: Insights from phase-field modeling. *Eng. Fract. Mech.* **2020**, *239*, 107301. [CrossRef]
24. Liu, Z.; Sun, Y.; Guo, W.; Li, Q. Reservoir-scale study of oil shale hydration swelling and thermal expansion after hydraulic fracturing. *J. Pet. Sci. Eng.* **2020**, *195*, 107619. [CrossRef]

25. Wang, L.; Yang, D.; Kang, Z. Evolution of permeability and mesostructure of oil shale exposed to high-temperature water vapor. *Fuel* **2021**, *290*, 119786. [CrossRef]
26. Huang, L.; Zhou, W.; Xu, H.; Wang, L.; Zou, J.; Zhou, Q. Dynamic fluid states in organic-inorganic nanocomposite: Implications for shale gas recovery and CO_2 sequestration. *Chem. Eng. J.* **2021**, *411*, 128423. [CrossRef]
27. Mohagheghian, E.; Hassanzadeh, H.; Chen, Z. Matrix-fracture transfer shape factor for modeling multimechanisitc multicomponent shale gas flow. *Int. J. Heat Mass Transf.* **2020**, *158*, 120022. [CrossRef]
28. Fan, K.; Dong, M.; Elsworth, D.; Li, Y.; Yin, C.; Li, Y. A dynamic-pulse pseudo-pressure method to determine shale matrix permeability at representative reservoir conditions. *Int. J. Coal Geol.* **2018**, *193*, 61–72. [CrossRef]
29. Heller, R.; Zoback, M. Laboratory measurements of matrix permeability and slippage enhanced permeability in gas shales. In Proceedings of the SPE/AAPG/SEG Unconventional Resources Technology Conference, Denver, CO, USA, 12–14 August 2013; URTEC: Houston, TX, USA, 2013; p. URTEC-1582659-MS.
30. Lu, T.; Xu, R.; Zhou, B.; Wang, Y.; Zhang, F.; Jiang, P. Improved method for measuring the permeability of nanoporous material and its application to shale matrix with ultra-low permeability. *Materials* **2019**, *12*, 1567. [CrossRef] [PubMed]
31. Qinhong, H.; Zhang, Y.; Xianghao, M.; Zheng, L.; Zhonghuai, X.; Maowen, L. Characterization of micro-nano pore networks in shale oil reservoirs of Paleogene Shahejie Formation in Dongying Sag of Bohai Bay Basin, East China. *Pet. Explor. Dev.* **2017**, *44*, 720–730.
32. Peng, S.; Loucks, B. Permeability measurements in mudrocks using gas-expansion methods on plug and crushed-rock samples. *Mar. Pet. Geol.* **2016**, *73*, 299–310. [CrossRef]
33. Hu, Z.; Deng, Y.; Li, J.; Wu, X.; Bai, J.; Tian, J. Modified experimental method to investigate micro transport in the shale matrix for shale gas production. *Front. Energy Res.* **2023**, *11*, 1260499. [CrossRef]
34. Wu, X.J.; Wang, Q.; Lyu, F.T.; Ning, Z.F.; Ren, Z.X. Experimental study on gas transport in shale matrix with real gas and Klinkenberg effects. *Geofluids* **2021**, *2021*, 5579307. [CrossRef]
35. Cui, X.; Bustin, A.M.M.; Bustin, R.M. Measurements of gas permeability and diffusivity of tight reservoir rocks: Different approaches and their applications. *Geofluids* **2010**, *9*, 208–223. [CrossRef]
36. Wu, X.; Ning, Z.; Qi, R.; Wang, Q.; Huang, L. Pore characterization and inner adsorption mechanism investigation for methane in organic and inorganic matters of shale. *Energy Fuels* **2020**, *34*, 4106–4115. [CrossRef]
37. Coppens, M.-O.; Dammers, A.J. Effects of heterogeneity on diffusion in nanopores—From inorganic materials to protein crystals and ion channels. *Fluid Phase Equilibria* **2006**, *241*, 308–316. [CrossRef]
38. Wu, K.; Li, X.; Wang, C.; Chen, Z.; Yu, W. Apparent permeability for gas flow in shale reservoirs coupling effects of gas diffusion and desorption. In Proceedings of the Unconventional Resources Technology Conference, Denver, CO, USA, 25–27 August 2014; Society of Exploration Geophysicists, American Association of Petroleum: Houston, TX, USA, 2014; pp. 2328–2345.
39. Liu, Z.; Yang, D.; Hu, Y.; Zhang, J.; Shao, J.; Song, S.; Kang, Z. Influence of in situ pyrolysis on the evolution of pore structure of oil shale. *Energies* **2018**, *11*, 755. [CrossRef]
40. Huang, H.; Yu, H.; Xu, W.; Lyu, C.; Micheal, M.; Xu, H.; Liu, H.; Wu, H. A coupled thermo-hydro-mechanical-chemical model for production performance of oil shale reservoirs during in-situ conversion process. *Energy* **2023**, *268*, 126700. [CrossRef]
41. Pan, Y.; Jia, Y.; Zheng, J.; Yang, S.; Bttina, H. Research progress of fracture development during in-situ cracking of oil shale. *J. Anal. Appl. Pyrolysis* **2023**, *174*, 106110. [CrossRef]
42. Gao, Q.; Cheng, Y.; Han, S.; Yan, C.; Li, Y.; Han, Z. Effect of shale matrix heterogeneity on gas transport during production: A microscopic investigation. *J. Pet. Sci. Eng.* **2021**, *201*, 108526. [CrossRef]
43. Javadpour, F.; Fisher, D.; Unsworth, M. Nanoscale Gas Flow in Shale Gas Sediments. *J. Can. Pet. Technol.* **2007**, *46*, 55–61. [CrossRef]
44. Civan, F. Effective correlation of apparent gas permeability in tight porous media. *Transp. Porous Media* **2010**, *82*, 375–384. [CrossRef]
45. Zhang, L.; Liang, H.; Zhao, Y.; Xie, J.; Peng, X.; Li, Q. Gas transport characteristics in shale matrix based on multiple mechanisms. *Chem. Eng. J.* **2020**, *386*, 124002. [CrossRef]
46. Wua, K.; Li, X.; Guo, C.; Chen, Z. Adsorbed gas surface diffusion and bulk gas transport in nanopores of shale reservoirs with real gas effect-adsorption-mechanical coupling. In Proceedings of the SPE Reservoir Simulation Symposium, Houston, TX, USA, 23–25 February 2015; Society of Petroleum Engineers: Richardson, TX, USA, 2015.

Disclaimer/Publisher's Note: The statements, opinions and data contained in all publications are solely those of the individual author(s) and contributor(s) and not of MDPI and/or the editor(s). MDPI and/or the editor(s) disclaim responsibility for any injury to people or property resulting from any ideas, methods, instructions or products referred to in the content.